Available online at www.sciencedirect.com
ScienceDirect
Trans. Nonferrous Met. Soc. China 22(2012) s585−s595
Transactions of Nonferrous Metals Society of China
www.tnmsc.cn

Effects of elastic-plastic properties of materials on residual indentation impressions in nano-indentation using sharp indenter

Jung-Min LEE[1], Chan-Joo LEE[1], Kyung-Hun LEE[2], Byung-Min KIM[3]

1. Dongnam Regional Division, Korea Institute of Industrial Technology, Busan 618-230, Korea;
2. Precision Manufacturing Systems Division, Pusan National University, Busan 609-735, Korea;
3. School of Mechanical Engineering, Pusan National University, Busan 609-735, Korea

Received 21 May 2012; accepted 19 November 2012

Abstract: One of the primary features of nano-indentation technique is that the contact area induced by an indenter is indirectly measured by a relationship between the penetration depth and the known geometry of the indenter. However, this indirect measurement occasionally leads to inaccurate properties of the indented material. The objective of this study is to investigate the effects of E^*/σ_r and the strain hardening exponents n of materials on the behaviors of pile-up and sink-in in nano-indentation and to predict n values of materials from the residual indentation impressions. The relations between the residual indentation profile and n value of the indented material were identified by dimensional analysis. Also, they were numerically formulated using FE analysis of nano-indentation for 140 different combinations of elastic-plastic parameters such as E, σ_y and n. The parameters of h_{rp}/h_m, h_{erp}/h_m, R_r/h_m and $H_{O\&P}/H_{real}$ were introduced as various dimensionless parameters to represent and quantify the residual indentation profile after indentation. They were subsequently characterized as dimensionless functions using n and E^*/σ_r values. Finally, the validity of these functions was verified through 3D FE analysis of nano-indentation for Al 6061-T6 and AISI 1010 materials.
Key words: nano-indentation; pile-up; sink-in; strain hardening exponent; FE simulation

1 Introduction

Nano-indentation technique is widely used as the simplest and most direct method to obtain the mechanical properties of materials in very small volumes, such as elastic modulus E, hardness H, yield stress σ_y and strain hardening exponent n [1−5]. One of the main features of the technique is that the contact area induced by an indenter is indirectly measured by a relationship between the penetration depth and the known geometry of the indenter without any optical observations of the residual indentation impression. However, this indirect measurement occasionally leads to inaccurate properties of the indented material. These errors are mostly caused by the formation of pile-up and sink-in in contact during indentation, which involve the increase and decrease in the true contact area, respectively [2]. BOLSHAKOV and PHARR [6] reported that the true contact area of a sharp indenter could be underestimated up to 60% for a certain material in the case of piling-up, thereby leading to similar errors in calculating material properties like E and H.

OLIVER and PHARR's method [7] was the most widely used to extract the contact (indentation) depth h_p of the indenter from an initial unloading slope dP_u/dh under load and is determined as

$$h_p = h_m - \xi \frac{P_m}{(dP_u/dh)_m} \quad (1)$$

where P_m and ξ are an indentation load at the indentation depth h_m and a geometric constant of the indenters, respectively [4]. The contact area A of Berkovich indenter is defined as $A=24.56h_p^2$. However, CHENG and CHENG [1] found that OLIVER and PHARR's method [7] is comparatively effective for most σ_y/E values when n is about 0.3 or when the ratio of σ_y/E (>0.05 for $0<n<0.5$) is very large.

The effects of pile-up and sink-in in indentation were studied by many researchers until now [1−3,6−13]. For

Foundation item: Project (2010-0008-277) supported by the NCRC (National Core Research Center) Program through the National Research Foundation of Korea, funded by the Ministry of Education, Science, and Technology, Korea; Project supported by R&D for Technology Development Program of Ministry of Knowledge Economy, Korea
Corresponding author: Byung-Min KIM; Tel: +82-51-5103074; E-mail: bmkim@pusan.ac.kr
DOI: 10.1016/S1003-6326(12)61770-1

the indentation of the materials in elastic region, the specimen surface typically tends to be sink-in. On the other hand, for the materials including elastic-plastic deformations, the behaviors of pile-up and sink-in are dependent on their E/σ_y and n values [1−4]. In general, the piling-up occurs when E/σ_y is extremely low or n is close to zero and sinking-in is dominant when n>0.3. Therefore, completely understanding and predicting the effects of pile-up and sink-in in indentation is crucial in extracting the accurate properties of the indented material [1].

This work was designed to investigate the effects of E^*/σ_r [5] and n values of materials on the behaviors of pile-up and sink-in in nano-indentation and to estimate n values of materials from the residual indentation impressions. Relations between the residual indentation profile and n of the indented material were defined by dimensional analysis. Also, they were numerically formulated as dimensionless functions of E^*/σ_r and n values using FE analysis of nano-indentation for 140 different combinations of elastic-plastic parameters such as E, σ_y and n. Finally, the validity of these functions was verified through 3D FE analysis of nano-indentation for Al 6061-T6 and AISI 1010 materials.

2 FE analysis of nano-indentation and definitions of pile-up and sink-in

2.1 FE analysis of nano-indentation

The FE simulations of nano-indentation were carried out for 140 different combinations of elastic-plastic parameters: E was varied from 10 GPa to 600 GPa, σ_y from 10 MPa to 2500 MPa, and n from 0.01 to 0.5 at 0.1 intervals, and Poisson ratio v was fixed at 0.3. For both Berkovich and Vickers indenters, the corresponding apex angle of their two dimensional cone is 70.3° [1]. The FE model of nano-indentation (Fig. 1) was assumed to be axisymmetric two-dimension and the indenter was modeled as a rigid body. The contact between the indenter and materials was defined to be frictionless [14]. The maximum indentation depth h_m was 1000 nm, where the size effect of the indented material is negligible [13]. All the simulations were performed using ABAQUS 6.3-1 based on large deformation theory [5,14,15].

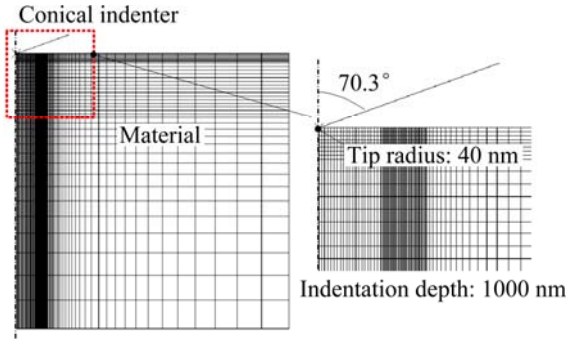

Fig. 1 FE model of nano-indentation using sharp indenter

Figure 2 shows the definitions of the contact boundary of pile-up and sink-in under full load and after complete unloading of the indenter in the FE simulations. h_p/h_m, h_{mp}/h_m, h_{rp}/h_m and R_r/h_m were defined as dimensionless parameters to express the amounts of pile-up and sink-in in indentation. Here, h_{rp} and R_r are the residual indentation depth and the residual contact radius by piling-up and sinking-in after unloading, respectively.

2.2 Definitions of pile-up and sink-in

The behaviors of elastic−plastic materials in an uniaxial tensile test can be expressed as a power law description. The power law true stress—true strain curve of materials can be assumed to be [1,5,15,16]:

$$\sigma=\begin{cases}E\varepsilon, \text{for } \varepsilon \le \dfrac{\sigma_y}{E}\\ K\varepsilon^n, \text{for}, \varepsilon \ge \dfrac{\sigma_y}{E}\end{cases} \tag{2}$$

where K is the strength coefficient. Continuity of the curve in Eq. (2) requires $K=\sigma_y(E/\sigma_y)n$ [1,5,15]. Therefore, E, n, σ_y and v are the independent parameters to describe the power law behavior of materials. Applying the reduced modulus $E^*(=[(1-v^2/E)+ (1-v_i^2/E_i)]^{-1}$, i is indenter's properties) and the representative stress σ_r, instead of E and σ_y, the behavior is represented as E, σ_r, v and n. Here, σ_r is a plastic stress characterized by a deformation of the indented material beneath a sharp indenter in indentation process and is independent of the strain hardening exponents of materials [1,5]. In this study, σ_r is defined based on LEE's research [15]. Using the dimensional analysis [5,15], the degrees of pile-up and sink-in are expressed as:

at h_m during loading,

$$\frac{h_p}{h_m}=\Pi_1\left(\frac{E^*}{\sigma_r},n\right) \tag{3}$$

and after unloading

$$\frac{h_{mp}}{h_m},\frac{h_{rp}}{h_m},\frac{R_r}{h_m}=\Pi_{2,3,4}\left(\frac{E^*}{\sigma_r},n\right) \tag{4}$$

3 Estimations of convective heat transfer coefficients (CHTC)

3.1 Effects of E^*/σ_r and n values on pile-up/sink-in

Figure 3 exhibits the effects of different E^*/σ_r and n values on the amounts of pile-up and sink-in h_p/h_m at full

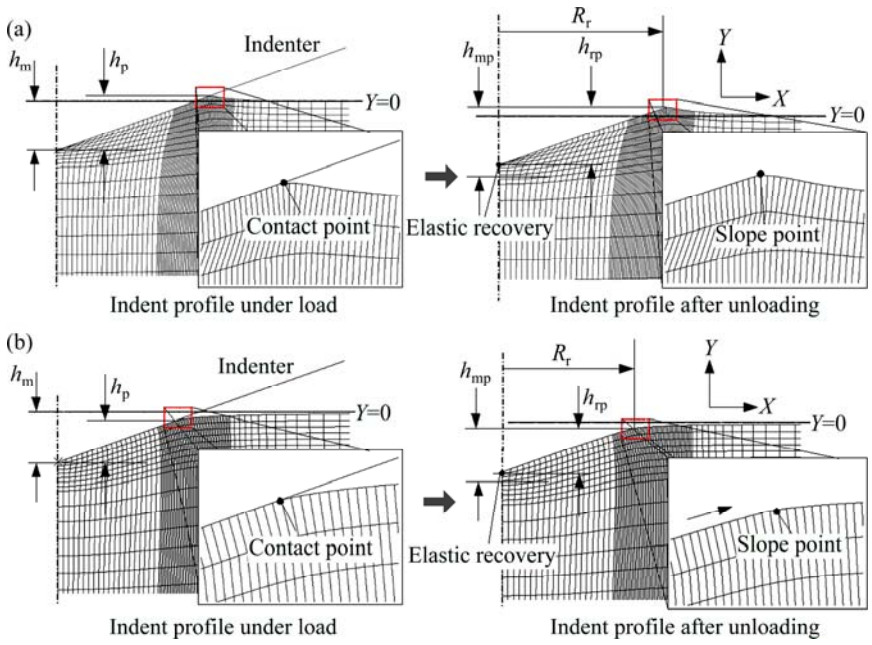

Fig. 2 Definitions of contact boundary of pile-up and sink-in under full load (a) and after complete unloading (b) of indenter

load. The amounts of h_p/h_m were clearly distinguished into the phenomena of pile-up and sink-in at n=0.3 approximately. The piling-up and sinking-in of materials were more dependent on their E^*/σ_r values than their n values in the range of E^*/σ_r<300 approximately. On the other hand, they relied entirely on their n values in E^*/σ_r<about 600. The phenomenon of sink-in was only observed, especially in E^*/σ_r<about 100.

Figure 4 shows the stress distributions of materials beneath the indenter for piling-up (E=500 GPa, σ_y=150 MPa, n=0.5) and sinking-in (E=240 GPa, σ_y=650 MPa, n=0.01) at full load and after complete unloading. In the piling-up, the plastic zone beneath the indenter at full load was much larger than the contact radius of the indenter. Also, the residual stress distributions after unloading were widely placed near the indenter and over the piled-up part. Especially, there was little the difference in the maximum stress values before and after unloading.

In sinking-in, the plastic zone and the stress distributions were limited within the contact radius and were more deeply formed than those of pile-up. Also, the maximum stress distributions were concentrated on the indenter tip at full load, whereas they were only observed on the sank-in part and the values were much lower than those at full load. In general, the amounts of elastic recovery and the differences in the stress values before and after unloading were much larger in sinking-in than in piling-up.

The approximate range of E^*/σ_r values for engineering metals with strain hardening properties are between 150 and 450 in Fig. 3. For the high strain hardening materials, the material within the plastic zone beneath the indenter becomes more hardened during indentation. As the indenter proceeds downward into the material, most of the plastic deformation occurs at the material around the plastic zone which is relatively softer. Therefore, the material near the indenter is observed to sink-in because the downward moving of the plastic zone by the indenter is more active during indentation [2,6]. For the low strain hardening materials, the moving of the plastic zone is blocked by its surrounding materials because the plastic zone is not hardened severely during indentation. Then, the material within the plastic zone moves toward free surface along the indenter surface where smaller deformation energy is required. Thus, the material near the indenter is observed to pile-up by this behavior of the plastic zone. The strain hardening materials, especially engineering metals, can be

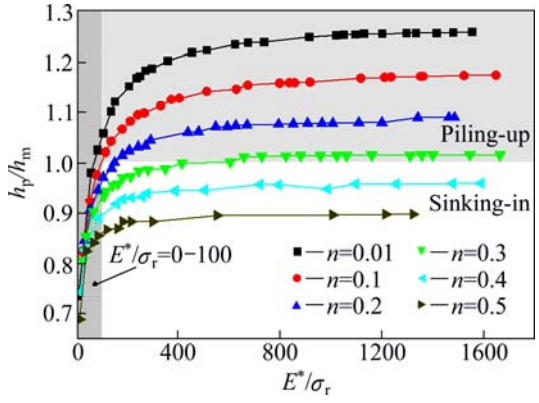

Fig. 3 Effect of different E^*/σ_r and n values on amounts of pile-up and sink-in h_p/h_m at full load

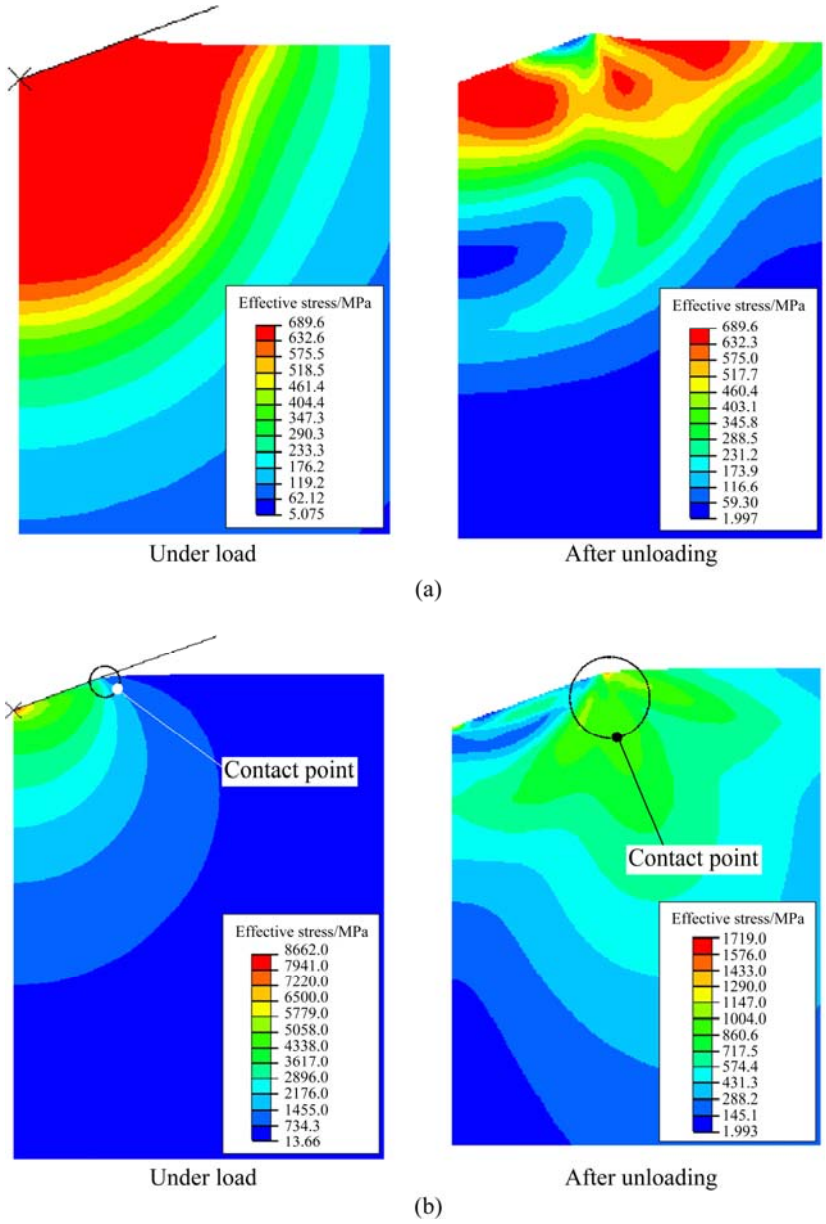

Fig. 4 Stress distributions beneath indenter for piled-up and sank-in materials at full load (a) and after complete unloading (b)

classified into piling-up and sinking-in around n=0.3.

The effects of different E^*/σ_r and n values on the amounts of pile-up and sink-in h_{mp}/h_m after unloading are shown in Fig. 5. The ratio of h_p/h_m was taken to quantitatively compare each amount of pile-up and sink-in at load in Fig. 3 and after unloading. Overall, piling-up was increased and sinking-in was released after unloading. These phenomena were much more obvious, especially in the range of E^*/σ_r<about 400. For n=0.3, the materials with E^*/σ_r<400 appeared to be sink-in at full load in Fig. 3 but were changed into pile-up after unloading. Especially, when E^*/σ_r<100 approximately, the phenomenon of sink-in during loading was dominant in most of the materials (Fig. 3). However, it was almost transformed to pile-up after unloading except some of

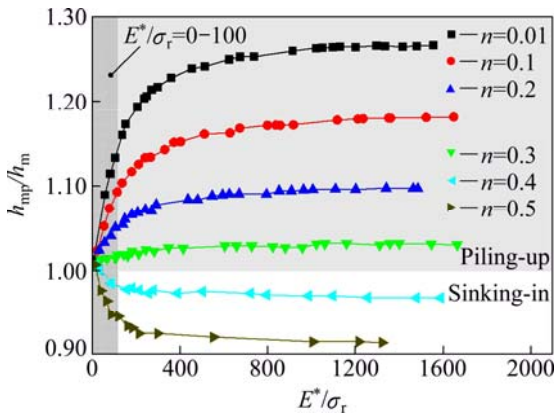

Fig. 5 Effects of different E^*/σ_r and n values on amounts of pile-up and sink-in h_{mp}/h_m after unloading

the materials with above n=0.4. These results are called the pseudo-pile-up by LI et al [16]. The material with very low E^*/σ_r values(E^*/σ_r<100) is likely to be similar to the characteristics of rubbers or elastomers which have an extremely high elastic strain.

Figure 6 shows the transition from sinking-in under full load to piling-up after complete unloading for the material with E=10 GPa, σ_y=750 MPa and n=0.01. The indentation profile at full load was placed down the original surface of the specimen (Y=0). However, after unloading the edge of the residual profile was displaced above the original surface by elastic recovery. In the case of the pseudo-pile-up, the pattern of the stress distribution under load was similar to that of sink-in in Fig. 4. However, the stress distributions below the indenter, which are almost a spherical shape, were more deeply and widely formed into the material and more narrowly placed within the contact radius than those of sink-in in Fig. 4. Also, there were the maximum stress distributions on the indenter tip after unloading unlike the sinking-in. This pseudo-piling-up may be often mistaken by observers for one of piled-up types in observations of the residual indentation impressions [16].

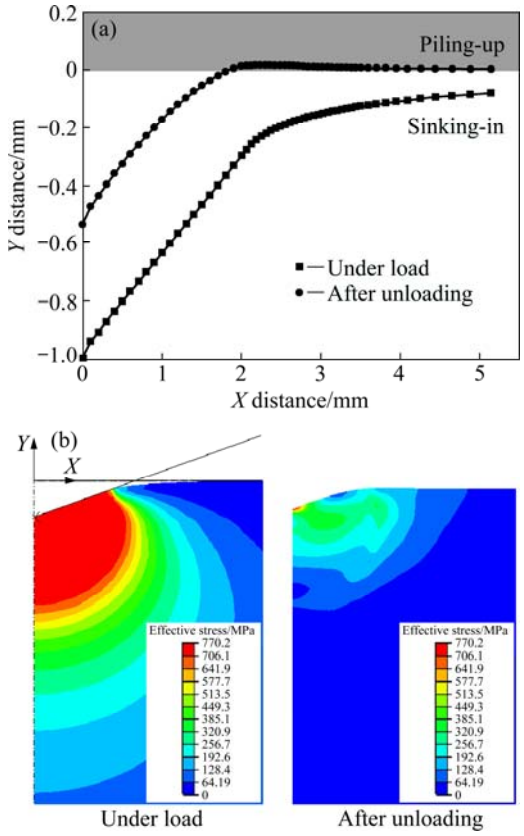

Fig. 6 Transition from sinking-in at full load to piling-up after complete unloading for pseudo-piled-up material

3.2 Quantifications of pile-up and sink-in after unloading

In Fig. 5 the behaviors and the phenomena of pile-up and sink-in can be easily distinguished and understood after unloading. However, the data are actually difficult to be approximated as one function. To solve this problem h_{rp}/h_m and R_r/h_m were introduced as dimensionless parameters to represent their phenomena and were expressed as functions of E^*/σ_r and n values after complete unloading in Figs. 7 and 8, respectively. Figures. 7 and 8 were numerically formulated as dimensionless Π_2 and Π_3 functions (Appendix A). Their closed forms were completed with fitting all 140 data points within ±3.0% errors.

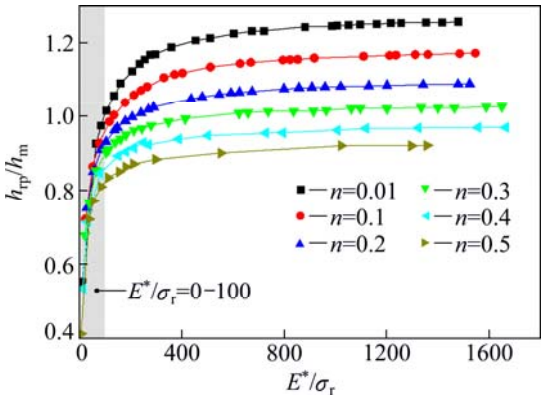

Fig. 7 Variations of h_{rp}/h_m as functions of E^*/σ_r and n values after complete unloading (dimensionless Π_2 function)

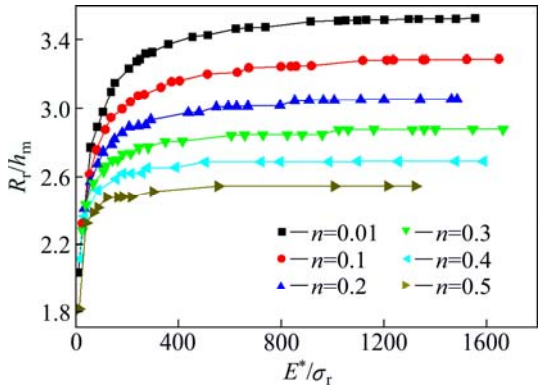

Fig. 8 Variations of R_r/h_m as functions of E^*/σ_r and n values after complete unloading (dimensionless Π_3 function)

Figure 9 shows the variations of $H_{O\&P}/H_{real}$ as functions of E^*/σ_r and n values after unloading. Here, $H_{O\&P}$ is the Oliver and Pharr's hardness calculated by the contact area $A_{O\&P}=24.56h_m^2$. H_{real} is the real hardness obtained by the real residual projected area $A_{real}=\pi R_r^2$ which was calculated from the FE simulations of nano-indentation. As shown in Fig. 9, $H_{O\&P}$ was overestimated (the underestimation of the contact area) for piling-up while it was underestimated (the overestimation of the contact area) for sinking-in, compared with H_{real}. Furthermore, $H_{O\&P}$ was completely underestimated in the range of E^*/σ_r<about 100 where

the phenomenon of sink-in appears to be nearly independent of n. When n=0.3 and E^*/σ_r<200 approximately, H_{real} was similar to $H_{O\&P}$. Especially, the differences between H_{real} and $H_{O\&P}$ were the maximum of 60% for piling-up when n=0.01 and E^*/σ_r>600 and 20% for sinking-in when n=0.5 except the region where E^*/σ_r values are below 100, respectively. These graphs were numerically formulated as dimensionless Π_4 function (Appendix A) in the same way as previously.

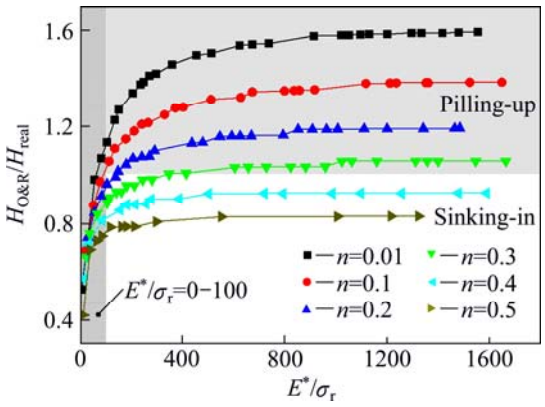

Fig. 9 Variations of $H_{O\&P}/H_{real}$ as functions of E^*/σ_r and n values after complete unloading (dimensionless Π_4 function)

4 Verifications of dimensionless functions

4.1 Geometrical definitions of pile-up from residual indentation profiles

Figure 10 shows the geometrical definitions for the residual indentation profiles of the piled-up material induced by the Berkovich indenter [13]. These definitions are premised on the assumption that the behavior of pile-up only appears along the flat faces of the indenter and not at corners. Also, the periphery of the piled-up material forms an arc along the triangle edge on the projected contact area. Hence, the projected contact area can be modeled as equilateral triangle bounded by arcs, as shown in Fig. 10. Here, A_{tpile} is the total projected area of the piled-up indentation impression after unloading which is calculated by the triangle and the areas enclosed by the arcs. A_{pile} is the extra area due to piling-up and $A_{O\&P}$ is the area determined using Oliver and Pharr's analysis. The width of the arc X_{pile} is equal to the projected width of the piled-up part. Thus, A_{tpile} can be calculated as $A_{tpile}=A_{O\&P}+3A_{pile}$ where $A_{O\&P}$ is given by

$$A_{O\&P}=\frac{1}{2}a\frac{a/2}{\tan(\theta/2)} \tag{5}$$

Under the assumption that $A_{O\&P}$ is the equilateral triangle (60°), the length of one side a of the triangle is then given by $a/2=(X_{tpile}-X_{pile})\tan\theta/2$. The contact radius R was calculated by measuring the dimension of the arc which is the three-point arc connecting both edges of a and X_{pile} on the center of a. Using R and a, the angle of the arc θ_R can be calculated by

$$\tan\frac{\theta_R}{2}=\frac{a/2}{R-X_{pile}} \quad \text{or} \quad \sin\frac{\theta_R}{2}=\frac{a/2}{R} \tag{6}$$

Thus, A_{pile} is given by

$$A_{pile}=\frac{\theta_R}{360}\pi R^2-\frac{1}{2}a(R-X_{pile}) \tag{7}$$

and h_{pile} and h_{rp} are finally expressed as follows

$$h_{pile}=\frac{X_{pile}}{\tan\theta'_{pile}} \quad \text{and} \quad h_{rp}=\frac{X'_{pile}}{\tan\theta'_{pile}} \tag{8}$$

The geometrical parameters of the residual indentation profile in Fig. 10 can be easily determined by the optical observations such as AFM and SEM [13].

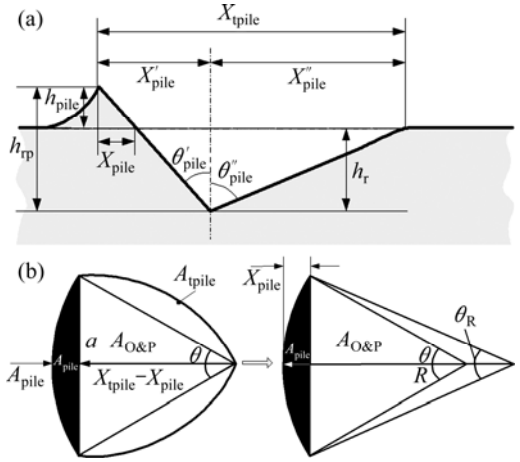

Fig. 10 Residual projected area and cross-sectional profile of piled-up materials by Berkovich indenter: (a) Cross-sectional view; (b) Plane view

Figure 11 shows the residual projected area and cross-sectional profile of the Berkovich indenter transformed to the equivalent-conical indenter. This area is called the equivalent-residual projected area in this study. Assuming that A_{tpile} is identical with the equivalent-residual projected area, A_{tpile} can be rewritten using the equivalent-residual contact radius R_{tpile} of the conical indenter as $A_{tpile}=A_{O\&P}+3A_{pile}=\pi R_{tpile}^2$. Thus, R_{tpile} is given as $R_{tpile}=[(A_{O\&P}+3A_{pile})/\pi]^{1/2}$. In Fig. 11, X_{epile} is then $R_{tpile}-R_{O\&P}$ where $R_{O\&P}$ is the equivalent-residual contact radius of $A_{O\&P}$ and is written as:

$$X_{epile}=\sqrt{\frac{A_{O\&P}+3A_{pile}}{\pi}}-\sqrt{\frac{A_{O\&P}}{\pi}} \tag{9}$$

where X_{epile} is the equivalent-residual width due to piling-up transformed to the conical indenter. Assuming that h_r of the Berkovich indenter is the same as that of the conical indenter, the equivalent-residual angle θ_{eq} is

defined as $\theta_{eq}=\tan^{-1}(R_{O\&P}/h_r)$. Thus, the equivalent-residual piled-up depth h_{epile} and the total equivalent-residual indentation depth h_{erp} are given as

$$h_{epile}=\frac{X_{epile}}{\tan\theta_{eq}},\quad h_{erp}=\frac{R_{tpile}}{\tan\theta_{eq}} \tag{10}$$

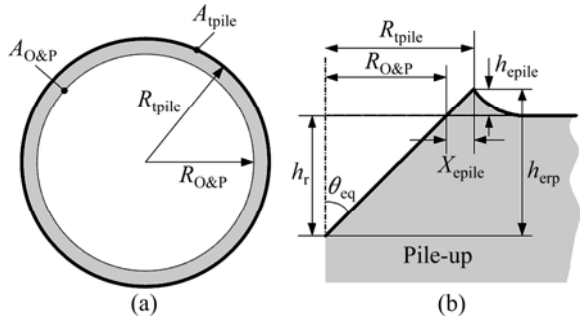

Fig. 11 Residual projected area and cross-sectional profile of piled-up by equivalent cone indenter: (a) Plane view; (b) Cross-sectional view

4.2 3D FE simulations of nano-indentation using Berkovich indenter

To verify the geometrical definitions of pile-up and dimensionless functions constructed in this study, 3D FE simulations of nano-indentation using the Berkovich indenter was performed. The 3D FE model was assumed to be 1/2 section of the indenter. Materials used in the 3D simulations are Al6061-T6 and AISI 1010, respectively. The elastic-plastic properties of each material were obtained from an uniaxial tensile tests and are listed in Table 1. Figure 12 shows the initial mesh system of 3D FE model and the configuration of the Berkovich indenter. General conditions for the 3D FE simulations of nano-indentation are identical with those of the previous 2D simulations in section 2.1.

Table 1 Mechanical properties of Al 6016-T6 and AISI 1010

Properties	E/GPa	σ_y/MPa	n
Al 6061-T6	70.6	331.7	0.081
AISI 1010	209.6	210.6	0.249

Figure 13 shows the stress distributions of the indentation impressions for Al 6061-T6 and AISI 1010 at full load and after unloading. The phenomenon of pile-up was clearly observed in both Al 6061-T6 and AISI 1010 because their n values are smaller than 0.3, which is an approximate base value to separate piling-up and sinking-in in engineering metals in Fig. 3. However, it was slightly smaller in AISI 1010 than in Al 6061-T6 by differences in their n and E^*/σ_r values. Figure 14 shows the residual indentation profiles of Al 6061-T6 and AISI 1010 obtained from 3D simulations. These data were used to define the geometries and the degrees of pile-up for each material.

4.3 Estimations of strain hardening exponents using Π_2, Π_3 and Π_4 functions

The geometrical definitions (marked in Figs. 10 and 11) and the dimensionless parameters (h_{rp}/h_m, h_{erp}/h_m, R_r/h_m and $H_{O\&P}/H_{real}$) of pile-up calculated from the residual indentation profiles (Fig. 14) for each material are summarized in Tables 2 and 3, respectively. Here, h_{rp} is the value directly extracted from the residual profiles. On the other hand, h_{erp} and R_r are the values converted into its equivalent-conical shape by equations in section 4.1. In addition to these, E^* and σ_r values of Al 6061-T6 and AISI 1010 that are necessary to use the dimensionless

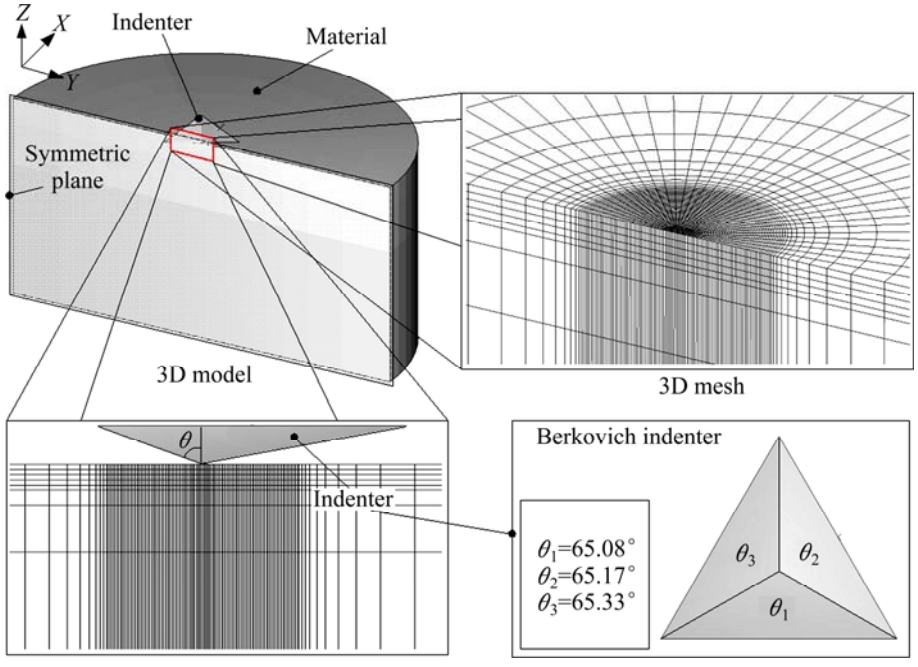

Fig. 12 Initial mesh system for 3D simulations of nano-indentation and shape of Berkovich indenter

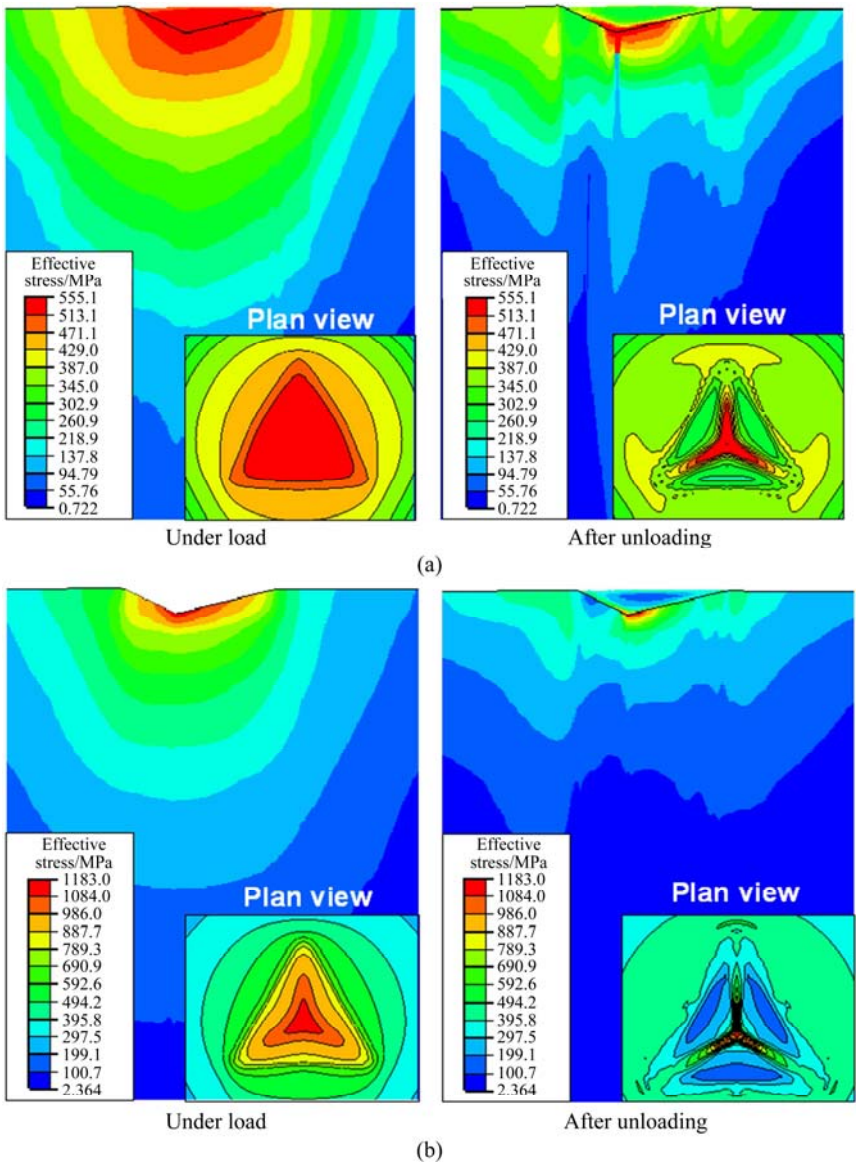

Fig. 13 Stress distributions of indentation impressions for Al 6061-T6 at full load and after unloading: (a) Al 6064-T6; (b) AISI 1010

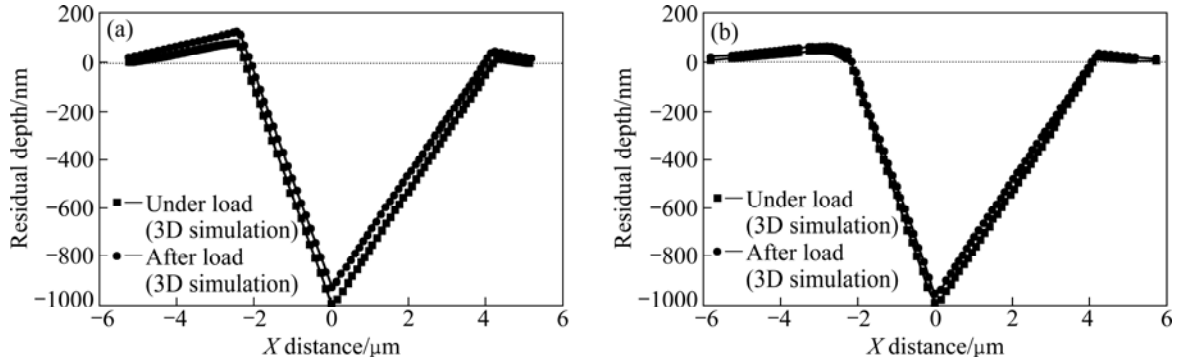

Fig. 14 Cross-sectional profiles of indentation impressions at full load and after unloading for Al 6061-T6 (a) and AISI 1010 (b)

functions established in section 3.2 were obtained from LEE's study [15].

The n values of Al 6061-T6 and AISI 1010 predicted using these parameters and dimensionless Π_2, Π_3 and Π_4 functions are listed in Table 4. The results showed that all the functions provided relatively exact n values which are within 10% errors in comparison with those of the tensile test. However, this margin of error was intensely variable with some measurement errors of the residual indentation profiles. Figure. 15 shows the

changes in n values with ±5% errors of the dimensionless parameters in Table 3. The n values in Fig. 15 are expressed as the percent relative error $((n_{\Pi}-n_{\text{tensile}})/n_{\text{tensile}}\times100\%)$ compared with those of the tensile test.

Overall, AISI 1010 was much less sensitive to the errors than Al 6061-T6. Also, the Π_4 function led to the smallest maximum and minimum deviations within the given errors. These differences in the sensitivity are mostly caused by E^*/σ_r values of each material and the ranges of the dimensionless parameters (h_{rp}/h_m, h_{erp}/h_m, R_r/h_m and $H_{O\&P}/H_{real}$) available at each functions. As illustrated in Figs. 7, 8 and 9, the range of the dimensionless parameters available at a given E^*/σ_r value becomes narrower as E^*/σ_r values decrease. Also, the ratio of $H_{O\&P}/H_{real}$ (Π_4 function) has a comparatively wider range of the applicable parameter at a certain E^*/σ_r value than others. For these reasons, the sensitivity to the measurement errors of the residual indentation profile is somewhat changed according to the Π functions and the materials used.

Table 2 Geometrical parameters of pile-up obtained from 3D simulations of nano-indentation

Property	Al 6061-T6	AISI 1010
$\theta_R/2$(°)	5.8066	2.8600
R/nm	37100.41	74510.36
X_{pile}/nm	190.361	92.807
X'_{pile}/nm	2430.30	2373.61
X''_{pile}/nm	4231.30	4150.50
h_{pile}/nm	90.558	39.457
h_r/nm	968.249	969.682
h_{rp}/nm	1056.81	1018.14
$a/2$/nm	3736.172	3713.116
A_{pile}/nm^2	1592514.50	803977.48
$A_{O\&P}$/nm^2	24177661.03	23880184.14
R_{tpile}/nm	3035.906	2892.929
$R_{O\&P}$/nm	2774.16	2757.05
X_{epile}/nm	261.742	135.884
θ_{eq}/(°)	70.760	70.722
h_{epile}/nm	91.354	47.792
h_{erp}/nm	1059.60	1017.47

Table 3 Dimensionless parameters of residual indentation profiles calculated from 3D simulations of nano-indentation

Property	Al 6061-T6	AISI 1010
E^*/σ_r	191.17	416.81
h_{rp}/h_m	1.0568	1.0181
h_{erp}/h_m	1.0596	1.0174
R_r/h_m	3.0359	2.892
$H_{O\&P}/H_{real}$	1.1976	1.1010

Table 4 n values of Al 6061-T6 and AISI 1010 predicted from 3D simulations of nano-indentation

Property	Al 6061-T6	AISI 1010
h_{rp}/h_m (Π_2)	0.079	0.251
h_{erp}/h_m (Π_2)	0.075	0.253
R_r/h_m (Π_3)	0.089	0.246
$H_{O\&P}/H_{real}$ (Π_4)	0.075	0.221

Figure 16 exhibits the variations of the indentation profiles according to measurement methods after unloading. In Fig. 16(a), the piled-up point in the indentation profile is not ideally sharp but very smooth curve. If the indentation profile is based on top point (profile A) or the inflection point (profile B), both the contact radius and the projected area may be over- or underestimated, respectively. In addition, the residual indentation depth also fluctuates according to how to choose the indentation profile. Actually, there are no definitive standard rules to define the shapes and the degrees of pile-up from the residual indentation impression.

Whether profile A or B is chosen, the change in h_{rp} will be almost smaller than that in X_{tpile}, which subsequently affects the calculations of R_r and A_{real}. However, as mentioned above, h_{rp}/h_m has a narrow range

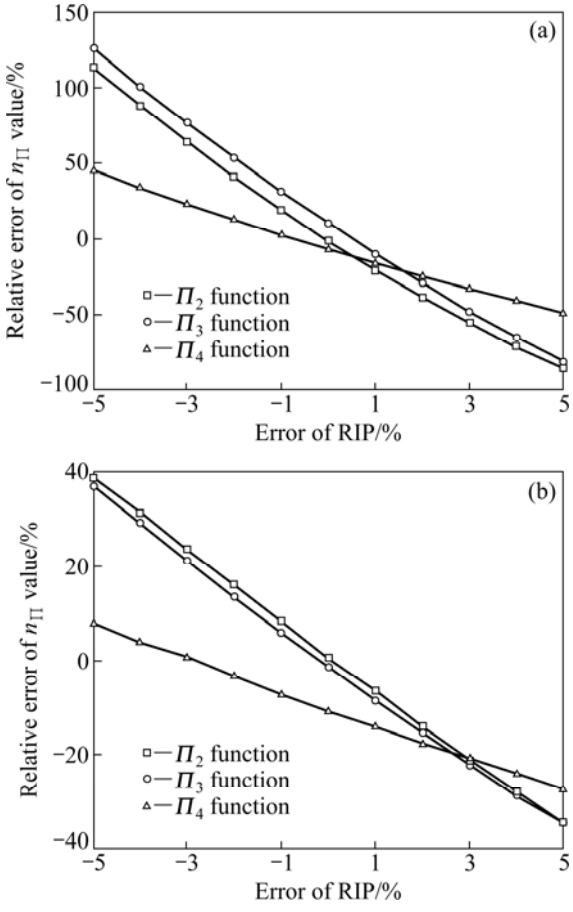

Fig. 15 Changes in n values with ±5% errors of dimensionless parameters: (a) Al 6064-T6; (b) AISI 1010

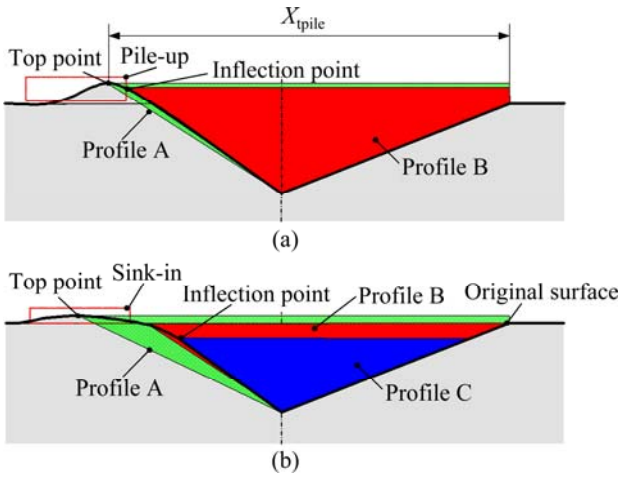

Fig. 16 Variations of indentation profiles according to measurement methods after unloading: (a) Pile-up; (b) Sink-in

of applications for a given E^*/σ_r value and R_r/h_m changes drastically with some measurement errors. In other words, if the choice of profile A or B leads to within ±5% errors for h_{rp}/h_m, it will actually exceed that range for R_r/h_m. Therefore, it is more desirable that profile A (the inflection point) is adopted as the residual indentation profiles to reduce errors in the predicted values from each function. Estimation of n values on the sank-in materials was not considered in this study. As shown in Fig. 16(b), the geometrical definitions on the sank-in amounts in the residual indentation profiles are very intricate and uncertain works. Thus, h_{erp}/h_m, R_r/h_m and $H_{O\&P}/H_{real}$ cannot be actually used and h_{rp}/h_m is only available as the dimensionless parameter to represent sinking-in. However, h_{rp}/h_m (Π_2 function) is very sensitive to the measurement errors and more changeable according to how to choose the indentation profiles than that of piling-up. To solve these problems, it is first necessary to determine the proper measurement method of the sank-in part. These problems, including the geometrical definitions of sink-in, will be discussed in further research in detail.

5 Conclusions

1) The indentation impressions of materials are divided into the phenomena of pile-up and sink-in at n=0.3 approximately. Also, the piling-up and sinking-in of materials are more dependent on their E^*/σ_r values than their n values in the range of E^*/σ_r<about 300. On the other hand, they rely entirely on their n values in E^*/σ_r>about 600. When E^*/σ_r<100 approximately, the phenomenon of sink-in mostly appears over all the materials independently of their n values at full load. However, it is inversely changed into pile-up after complete unloading. This effect is called the pseudo-pile-up and is dominant in the range of extremely small E^*/σ_r.

2) The real hardness H_{real} calculated from the real residual projected area is underestimated up to a maximum of 60% at n=0.01 for pile-up and is over-estimated up to a maximum of 20% at n=0.5 for sink-in except the region where E^*/σ_r values are below 100, respectively, in comparison with OLIVER and PHARR's hardness $H_{O\&P}$.

3) The dimensionless Π_2, Π_3 and Π_4 functions provide the estimation of n values within 10% error from the residual indentation profiles of Al 6061-T6 and AISI 1010 obtained from 3D simulations of nano-indentation. However, the smaller the indented material has E^*/σ_r value, the more these functions are sensitive to the measurement error of the residual indentation profile. This is because the range of the dimensionless parameters (h_{rp}/h_m, h_{erp}/h_m, R_r/h_m and $H_{O\&P}/H_{real}$) at a given E^*/σ_r value grows progressively narrower as E^*/σ_r values decrease. Also, the shape and the degree of pile up should be defined based on the inflection point of the piled-up part in the residual indentation profiles to minimize the error of the dimensionless functions.

4) As the above result, a series of dimensionless functions constructed in this study are expected to help conveniently understand and predict an approximate strain hardening exponent of the material in very small volumes such as thin films, coatings, microelectronic devices and MEMS.

Appendix A

$$\frac{h_{rp}}{h_m}=\Pi_2\left(\frac{E^*}{\sigma_r},n\right)=$$

$$(0.81337n^3-0.47142n^2+0.08989n-0.0012)\ln\left(\frac{E^*}{\sigma_r}\right)^3+$$

$$(-13.1679n^3+7.56303n^2-1.42724n-0.01267)\ln\left(\frac{E^*}{\sigma_r}\right)^2+$$

$$(69.70148n^3-39.6247n^2+7.26262n+0.35985)\ln\left(\frac{E^*}{\sigma_r}\right)+$$

$$(-122.25n^3+69.1623n^2-12.6147n-1.25403)$$

$$\frac{R_r}{h_m}=\Pi_3\left(\frac{E^*}{\sigma_r},n\right)=$$

$$(0.38148n^3-0.26298n^2+0.05868n-0.00251)\ln\left(\frac{E^*}{\sigma_r}\right)^3+$$

$$(-6.30333n^3+4.3315n^2-0.93507n+0.0184)\ln\left(\frac{E^*}{\sigma_r}\right)^2+$$

$$(34.37749n^3-23.5298n^2+4.75311n+0.11394)\ln\left(\frac{E^*}{\sigma_r}\right)+$$

$$(-63.0245n^3+43.25339n^2-8.44153n+0.42756)$$

$$\frac{H_{\mathrm{O\&P}}}{H_{\mathrm{real}}}=\Pi_4\left(\frac{E^*}{\sigma_{\mathrm{r}}},n\right)=$$

$$(0.76279n^3-0.5258n^2+0.11732n-0.00501)\ln\left(\frac{E^*}{\sigma_{\mathrm{r}}}\right)^3+$$

$$(-12.6057n^3+8.66216n^2-1.86997n+0.0368)\ln\left(\frac{E^*}{\sigma_{\mathrm{r}}}\right)^2+$$

$$(68.754481n^3-47.059n^2+9.50609n+0.22788)\ln\left(\frac{E^*}{\sigma_{\mathrm{r}}}\right)+$$

$$(-126.048n^3+86.50599n^2-16.8828n-1.20129)$$

References

[1] CHENG Y T, CHENG C M. Scaling, dimensional, and indentation measurements [J]. Material Science and Engineering R, 2004, 44: 91−149.

[2] FISCHER-CRIPPS A C. Nanoindentation [M]. New York: Springer-Verlag, 2002.

[3] FISCHER-CRIPPS A C. Introduction to contact mechanics [M]. New York: Springer-Verlag, 2002.

[4] RIETH M, SCHOMMER W. Handbook of Theoretical and computational nanotechnology Vol. 4 [M]. Los Angeles: American Scientific Publishers, 2004: 387−461.

[5] DAO M, CHOLLACOOP N, van VLIET K J, VENKATESH T A, SURESH S. Computational modeling of the forward and reverse problems in instrumented sharp indentation [J]. Acta Materialia, 2001, 49: 3899−3918.

[6] BOLSHAKOV A, PHARR G M. Influence of piling-up on the measurement of mechanical properties by load and depth sensing indentation techniques [J]. Journal of Material Research, 1998, 13(4): 1049−1058.

[7] OLIVER W C, PHARR G M. An improved technique for determining hardness and elastic-modulus using load and displacement sensing indentation experiments [J]. Journal of Materials Research, 1992, 7(6): 1564−1583.

[8] LI Z C, KESE K. Semi-ellipse method for accounting for the pile-up contact area during nanoindentation with the Berkovich indenter [J]. Scripta Materialia, 2006, 55(8): 699−702.

[9] GARRIDO MANEIRO M A, RODRIGUEZ J. Pile-up effect on nanoindentation tests with spherical-conical tips [J]. Scripta Materialia, 2005, 52(7): 593−598.

[10] RODRIGUEZ J, GARRIDO M A. A procedure to prevent pile-up effects on the analysis of spherical indentation data in elastic-plastic materials [J]. Mechanics of materials, 2007, 39(11): 987−997.

[11] DAS G, Ghosh S, Ghosh S, Ghosh R N. Materials characterization and classification on the basis of materials pile-up surrounding the indentation [J]. Materials Science & Engineering A, 2005, 408: 158−164.

[12] MCELHANEY K W, VLASSAK J J, NIX W D. Determination of indenter tip geometry and indentation contact area for depth-sensing indentation experiments [J]. Journal of Material Research, 1998, 13(5): 1300−1306.

[13] TALJAT B, PHARR G M. Development of pile-up during spherical indentation of elastic-plastic solids [J]. International Journal of Solids and Structures, 2004, 41(14): 3891−3904.

[14] BUCAILLE J L, STAUSS S, FELDER E, MICHLER J. Determination of plastic properties of metals by instrumented indentation using different sharp indenters [J]. Acta Materialia, 2003, 51(6): 1663−1678.

[15] LEE J M, LEE C J, KIM B M. Reverse analysis of nano-indentation using different representative strains and residual indentation profiles [J]. Material & Design, 2009, 30(9): 3395−3404.

[16] LI Z, CHENG Y T, YANG H T, CHANDRASEKAR S. On two indentation hardness definitions [J]. Surface & Coatings Technology, 2002, 154(2−3): 124−130.

(Edited by HE Xue-feng)